Numerical investigation of a mistuned industrial bladed disk dynamics with structural contacts using time and frequency methods

Florence Nyssen, Yann Colaitis, Alain Batailly

To cite this version:

Florence Nyssen, Yann Colaitis, Alain Batailly. Numerical investigation of a mistuned industrial bladed disk dynamics with structural contacts using time and frequency methods. Journal of Sound and Vibration, 2022. hal-03694099

Numerical investigation of a mistuned industrial bladed disk dynamics with structural contacts using time and frequency methods

Nyssen F., Colaïtis Y., Batailly A.[1]

Abstract

This work focuses on the numerical investigation of mistuned bladed disk dynamics undergoing blade-tip/casing contact events. The effect of mistuning on the bladed disk dynamics is evaluated as it undergoes structural blade-tip/casing contacts in the vicinity of its nominal angular speed. It is first underlined that the interaction of interest is in essence a rubbing interaction involving all the blades with no significant disk response. Indeed, results obtained with a single blade model and the full bladed disk suggest that both contact stiffening and maximum displacements are similar for both models. Then, an in-depth analysis of the tuned bladed disk interaction is carried out using both time and frequency solution methods. The analysis of the tuned bladed disk highlights that contact stiffening and maximum amplitudes may be underestimated by time integration strategies. Numerical challenges inherent to frequency methods are then underlined on mistuned bladed disks. A stochastic analysis on the influence of mistuning in a nonlinear context is carried out using time integration strategy. Amplification and localization factors are computed to quantify the effect several degrees of mistuning on the bladed disk dynamics with contact nonlinearities. Due to the inherent restrictions associated with the employed time integration methods, the analysis is centered on localization factors. It is evidenced that two areas of high localization stand out, all located close to sudden changes of amplitudes, thus suggesting the possible coexistence of distinct stable solutions featuring very distinct levels of localization.

Keywords

rotor/stator contact interaction, time integration, harmonic balance method, mistuning, localization factor, amplification factor

1 - Department of Mechanical Engineering, École Polytechnique de Montréal, P.O. Box 6079, Succ. Centre-Ville, Montréal, Québec, Canada H3C 3A7

Investigation numérique de la dynamique d'un disque aubagé industriel désaccordé avec contacts structurels par méthodes temporelle et fréquentielle

Nyssen F., Colaïtis Y., Batailly A.[1]

Résumé

Ce travail se focalise sur l'investigation numérique de la dynamique d'un disque aubagé désaccordé soumis à des contacts aube/carter. L'effet du désaccordage sur la dynamique du disque aubagé est évalué lorsqu'il est soumis à des contacts structurels entre le bout d'aube et le carter à proximité de sa vitesse angulaire nominale. Il est d'abord souligné que l'interaction d'intérêt est par essence une interaction de frottement impliquant toutes les aubes sans participation significative du disque. En effet, les résultats obtenus avec un modèle d'aube seule et avec le disque aubagé complet suggèrent qu'à la fois le raidissement au contact et les déplacements maximum sont similaires pour les deux modèles. Ensuite, une analyse approfondie de l'interaction du disque aubagé accordé est menée au moyen de méthodes temporelle et fréquentielle. L'analyse du disque aubagé accordé montre que le raidissement au contact et les amplitudes maximales pourraient être sous-estimées par les stratégies d'intégration temporelle. Des défis inhérents aux méthodes fréquentielles sont ensuite soulignées pour les disques aubagés désaccordés. Une étude stochastique de l'influence du désaccordage dans un contexte nonlinéaire est menée en utilisant la stratégie d'intégration temporelle. Les facteurs d'amplification et de localisation sont calculés pour quantifier l'effet de différents degrés de désaccordage sur la dynamique du disque aubagé avec nonlinéarités de contact. Étant donné les restrictions inhérentes associées aux méthodes d'intégration temporelles, l'analyse est centrée sur les facteurs de localisation. Il est mis en évidence que deux zones de forte localisation ressortent, proches des changements soudain d'amplitudes, ce qui suggère la possible coexistance de solutions stables distinctes présentant des niveaux de localisation très distincts.

Mots-clés

interaction de contact rotor/stator, intégration temporelle, méthode d'équilibrage harmonique, désaccordage, facteur de localisation, facteur d'amplification

1 - Département de génie mécanique, École Polytechnique de Montréal, P.O. Box 6079, Succ. Centre-Ville, Montréal, Québec, Canada H3C 3A7

1 Introduction

Among the avenues considered for lowering the environmental footprint of modern aircraft engines, engineers have been focusing on two promising design solutions: (1) the use of lighter materials, and (2) the reduction of operating clearances. While the first solution mostly relates to the development of new materials—such as composite fibers [1] or ceramic composite matrix materials in high pressure turbines [2]—, the second solution may advantageoulsy yield performance increase on current engines. In particular, the reduction of nominal clearances between rotating bladed disks and their surrounding casing [3] prevents recirculating air flow at the tip of the blades which improves the overall aerodynamic performances of the engine. However, reducing clearances unavoidably favors the occurrence of blade-tip/casing contact events, to a point where these events must now be accounted for in non-accidental configurations [4, 5].

Blade-tip/casing contact interactions are typically divided into three categories: rubbing interactions [3, 6, 7], modal interactions [8, 9], and whirl motions [10, 11]. Beside of usually high wear levels on the abradable coating—a sacrificial material deposited along the casing contact surface to decrease the severity of blade-tip/casing contacts [12, 13]—, rubbing interactions involve a single blade that experiences significant amplitudes of vibration (oftentimes leading to blade failure) but there is usually no significant vibration of the disk or casing. Modal interactions however involve a full bladed disk and its surrounding casing: vibration modes of both structures feature the same number of nodal diameters so that the casing and the bladed disk may exchange energy through repeated contacts. Finally, whirl motions refer to orbital motions in accidental configurations, following bearing failure for instance. These interactions involve a full bladed disk and significant shaft motions so that they require a precise modelling of inertial effects.

The understanding of blade-tip/casing contact interactions has motivated a variety of experimental and numerical investigations over the past decades. On the experimental front, full-scale experiments are extremely costly. Therefore, designed test benches usually focus on the characterization of specific phenomena. In particular, wear mechanisms of the abradable layer [12, 14, 15, 16, 17] and blade dynamics [18, 19, 20, 21, 22] have been investigated. Because single blade contact interactions have been observed experimentally, published works mostly focus on rubbing interactions [3, 6, 7]. Published experimental data for modal [8] or whirl interactions is very scarce.

From a numerical standpoint, a variety of modelling strategies have been developed to simulate and predict blade-tip/casing contact interactions. Phenomenological models [23, 9, 24] and full 3D finite element industrial models combined with reduced-order modelling techniques [25] have been employed depending on the specificities of each type of interaction. For rubbing interaction for instance, the progressive wear of the abradable layer is key and a precise modelling of the blade-tip/casing clearance evolution is required to accurately predict the dynamics of the blade [26]. So far, time integration strategies have been the workhorse of researchers for the modelling of rubbing interactions and recent publications underlined the good agreement between numerical results and experimental observations [27, 2]. The increasing efficiency and accuracy of numerical methodologies dedicated to blade-tip/casing contacts makes it possible to foresee their applications within the design stage of blades and bladed disks. However, several roadblocks remain, including the lack of research on the combination of nonlinear structural contact interactions with key issues of blade disk design such as mistuning.

Mistuning relates to discrepancies between each blade of a bladed disk. In the scientific literature, several types of mistuning are considered: small mistuning [28] due to manufacturing tolerances or material inhomogeneities, large mistuning related to wear or blade damage [28] and intentional mistuning [29, 30]. In this paper, the focus is made on small mistuning only. The effect of small mistuning on a bladed disk dynamics has been widely studied in a linear context [28]. The main effects are frequency splitting [31] leading to a high modal density, vibration amplifications [32, 33] and localization of the vibration energy [34, 35] that reduces a bladed disk lifespan [36]. Key quantities of interest are (1) the amplification factor [32], usually defined as the ratio between the maximum response of the system in the mistuned configuration and in the tuned one, and (2) the localization factor [37] that allows to quantify the energy localization within the bladed disk. In order to analyze the influence of mistuning on industrial bladed disks, dedicated reduced-order modelling techniques have been developed [38, 39, 40].

Due to the random nature of mistuning, stochastic analyzes are required to quantify its effect on a bladed disk dynamics. Both Monte Carlo simulations [33] or more recent alternative solutions such as polynomial chaos expansion [41, 42, 43] have been used. As mentioned above, the literature is still very scarce with respect to the combined analysis of mistuning and nonlinear structural interactions, be it related to blade-root friction dampers [44, 45, 46, 47] or blade-tip contacts [48, 49].

This work aims specifically at providing a better understanding of the influence of mistuning in the context of rubbing interactions, using both time and frequency solution methods. The paper is organized as follows. In the first section, the employed methodologies are presented. In particular, the reduced-order modelling techniques for a single blade and a bladed disk model are recalled. The emphasis is made on the management of mistuning within reduced-order models (ROM) featuring nonlinear mechanical interfaces. In the second section, the focus is made on the definition of rubbing interactions for a full bladed disk. Two finite element models—a single blade and a full bladed disk—are presented and the interaction of interest is detailed. In the third section, two solution paradigms—based on the harmonic balance method in the frequency domain [50] and time integration [51]—are considered to capture the bladed disk vibration response. The comparison of the two solution paradigms is carried out on both tuned and mistuned models. Finally, a stochastic analysis of the influence of mistuning on the bladed disk dynamics is carried out using the time integration strategy in the last section.

2 Methodology

The problem of interest consists in a bladed disk that rotates around its axis of rotation at constant angular speed and that impacts the surrounding casing assumed perfectly rigid. The bladed disk is modeled using a 3D finite element model. The equation of motion of this nonlinear system may be written as follows:

$$\mathbf{M}\ddot{\mathbf{x}} + \mathbf{D}\dot{\mathbf{x}} + \mathbf{K}\mathbf{x} + \mathbf{f}_{\mathrm{c}}(\mathbf{x}, \dot{\mathbf{x}}) = \mathbf{f}_{\mathrm{ext}}(\Omega, t) \tag{1}$$

where $\mathbf{M}$, $\mathbf{D}$ and $\mathbf{K}$ stand for the mass, damping and stiffness structural matrices, $\mathbf{x}$ is the displacement vector, and $\mathbf{f}_{\mathrm{c}}$ and $\mathbf{f}_{\mathrm{ext}}$ respectively refer to the contact forces and the external forces. As a first step towards a better understanding of the influence of mistuning in a nonlinear context, inertial and thermal effects are neglected. A modal damping is considered.

2.1 Model reduction

The large size of industrial finite element models calls for model reduction techniques to solve the equation of motion in an efficient manner. The Craig-Bampton reduction method [52] is considered as it advantageously allows to retain physical degrees of freedom within the reduced space for contact treatment. This reduction method relies on the construction of a projection matrix made of constraint modes and fixed-interface modes to reduce the size of the problem. Its straightforward application in the case of a single blade model is not recalled here for the sake of brevity. However, specific adjustments required for its application to a full bladed disk, be it tuned or mistuned, are recalled below.

2.1.1 Tuned bladed disk

Building the reduced order model of the full tuned bladed disk takes advantage of its cyclic symmetry. The bladed disk counts N identical sectors. Key steps of the reduction method presented [53] are briefly recalled in this section.

The finite element model of a reference sector of the bladed disk is partitioned into internal (subscript i), boundary (subscript b) and cyclic (subscript c) degrees of freedom. Structural matrices of this reference sector then reads:

$$\mathbf{Y}_{\mathrm{s}} = \begin{bmatrix} \mathbf{Y}_{\mathrm{ii}} & \mathbf{Y}_{\mathrm{ib}} & \mathbf{Y}_{\mathrm{ic}} \\ \mathbf{Y}_{\mathrm{bi}} & \mathbf{Y}_{\mathrm{bb}} & \mathbf{Y}_{\mathrm{bc}} \\ \mathbf{Y}_{\mathrm{ci}} & \mathbf{Y}_{\mathrm{cb}} & \mathbf{Y}_{\mathrm{cc}} \end{bmatrix}, \qquad \mathbf{Y} = \{\mathbf{K}, \mathbf{M}\} \tag{2}$$

The cyclic symmetry property of the bladed disk implies that its structural matrices are block-circulant in polar coordinates:

$$\mathbf{Y} = \begin{bmatrix} \mathbf{Y}_0 & \mathbf{Y}_1^\intercal & \mathbf{0} & \dots & \mathbf{Y}_1 \\ \mathbf{Y}_1 & \mathbf{Y}_0 & \mathbf{Y}_1^\intercal & \mathbf{0} & \dots \\ & & \ddots & & \\ \mathbf{0} & \dots & \mathbf{Y}_1 & \mathbf{Y}_0 & \mathbf{Y}_1^\intercal \end{bmatrix} \quad \text{with} \quad \mathbf{Y}_0 = \begin{bmatrix} \mathbf{Y}_{\text{ii}} & \mathbf{Y}_{\text{ib}} \\ \mathbf{Y}_{\text{bi}} & \mathbf{Y}_{\text{bb}} \end{bmatrix} \quad \text{and} \quad \mathbf{Y}_1 = \begin{bmatrix} \mathbf{Y}_{\text{ic}} & \mathbf{0} \\ \mathbf{Y}_{\text{bc}} & \mathbf{0} \end{bmatrix} \tag{3}$$

The structural matrices can be block-diagonalized by means of the Fourier matrix $\mathcal{F}$ (Bdiag refers to a block-diagonal matrix):

$$\hat{\mathbf{Y}} = \mathcal{F}^\intercal \mathbf{Y} \mathcal{F} = \text{Bdiag}\left(\hat{\mathbf{Y}}^{(n_d)}\right), \quad n_d = 0, 1, \dots, \lfloor \frac{N}{2} \rfloor \tag{4}$$

in which each block $\hat{\mathbf{Y}}^{(n_d)}$ corresponds to the nodal diameter n_d and reads [54]:

$$\hat{\mathbf{Y}}^{(n_d)} = \begin{bmatrix} \mathbf{Y}_0 + (\mathbf{Y}_1 + \mathbf{Y}_1^\intercal)\cos(n_d \frac{2\pi}{N}) & (\mathbf{Y}_1 - \mathbf{Y}_1^\intercal)\sin(n_d \frac{2\pi}{N}) \\ (\mathbf{Y}_1^\intercal - \mathbf{Y}_1^\intercal)\sin(n_d \frac{2\pi}{N}) & \mathbf{Y}_0 + (\mathbf{Y}_1 + \mathbf{Y}_1^\intercal)\cos(n_d \frac{2\pi}{N}) \end{bmatrix} \tag{5}$$

Reduced nodal diameter matrices are then obtained by means of a projection using transfer matrix $\hat{\mathbf{\Phi}}_\eta^{(n_d)}$:

$$\hat{\mathbf{Y}}_{\text{r}}^{(n_d)} = \left(\hat{\mathbf{\Phi}}_\eta^{(n_d)}\right)^\intercal \hat{\mathbf{Y}}^{(n_d)} \hat{\mathbf{\Phi}}_\eta^{(n_d)} \qquad \text{with} \qquad \hat{\mathbf{\Phi}}_\eta^{(n_d)} = \begin{bmatrix} \mathbf{I} & \mathbf{0} \\ \hat{\mathbf{\Psi}}_{\text{s}}^{(n_d)} & \hat{\mathbf{\Psi}}_{\text{c}}^{(n_d)} \end{bmatrix} \tag{6}$$

in which $\hat{\mathbf{\Psi}}_{\text{s}}^{(n_d)}$ and $\hat{\mathbf{\Psi}}_{\text{c}}^{(n_d)}$ contain the constraint and η fixed-interface modes. The final reduced matrices read:

$$\mathbf{Y}_{\text{r}} = \mathcal{F} \ \text{Bdiag}\left(\hat{\mathbf{Y}}_{\text{r}}^{(n_d)}\right) \mathcal{F}^\intercal \tag{7}$$

2.1.2 Mistuned bladed disk

Mistuning is introduced directly within the tuned ROM using a modified version of the Component Mode Mistuning (CMM) method for small mistuning [55]. This method allows to retain a combination of modal coordinates and physical degrees of freedom for contact treatment in the mistuned ROM. It relies on the assumption that the blade's displacements are very small at its root so that the whole blade's displacement field may be accurately described with a combination of clamped blade modes. No additional assumption on the retained physical degrees of freedom is made. Two sets of matrices are used in the method: (1) the tuned reduced matrices $\mathbf{K}_{\text{r}}$ and $\mathbf{M}_{\text{r}}$ obtained from Eq. (7) with their eigenfrequencies and eigenvectors denoted $\mathbf{\Lambda}_{\text{r}}$ and $\mathbf{\Phi}_{\text{r}}$, and (2) the structural matrices related to the restriction of the finite element model of the reference sector to the blade only, clamped at its root and denoted $\mathbf{K}_{\text{b}}$ and $\mathbf{M}_{\text{b}}$, with the corresponding eigenfrequencies and eigenvectors denoted $\mathbf{\Lambda}_{\text{b}}$ and $\mathbf{\Phi}_{\text{b}}$.

Mistuning is applied in the modal space of the clamped blade model, restricted to the first R vibration modes. Parameter R is called the restriction parameter. It is assumed that clamped blade free-vibration modes are consistent with those of the blade belonging to the full bladed disk model, *i.e.* that the displacement at the blade root is negligible. The restriction of $\mathbf{\Lambda}_{\text{b}}$ and $\mathbf{\Phi}_{\text{b}}$ to the R first modes is noted $\mathbf{\Lambda}_{\text{b}}|_R$ and $\mathbf{\Phi}_{\text{b}}|_R$.

The mistuned reduced stiffness and mass matrices are obtained by a projection of the modal structural matrices $\boldsymbol{\kappa}$ and $\boldsymbol{\mu}$ such as:

$$\mathbf{K}_{\text{r}}^\delta = \left(\mathbf{\Phi}_{\text{r}}^{-1}\right)^\intercal \boldsymbol{\kappa} \mathbf{\Phi}_{\text{r}}^{-1} \qquad \text{and} \qquad \mathbf{M}_{\text{r}}^\delta = \left(\mathbf{\Phi}_{\text{r}}^{-1}\right)^\intercal \boldsymbol{\mu} \mathbf{\Phi}_{\text{r}}^{-1} \tag{8}$$

where the modal structural matrices read:

$$\boldsymbol{\kappa} = \mathbf{\Lambda}_{\text{r}} + \begin{bmatrix} \mathbf{\Lambda}^\delta & \mathbf{0} \\ \mathbf{0} & \mathbf{0} \end{bmatrix} \qquad \text{and} \qquad \boldsymbol{\mu} = \mathbf{I} \tag{9}$$

in which $\mathbf{\Lambda}^{\delta}$ is the deviation due to mistuning. The deviation can be computed using:

$$\mathbf{\Lambda}^{\delta} = \sum_{i=1}^{N} \delta_i \mathbf{Q}_i^{\intercal} \mathbf{\Lambda}_{\mathrm{b}}|_R \mathbf{Q}_i \tag{10}$$

with δ_i the mistuning of blade i and $\mathbf{Q}_i$ the participation factor of blade i given by:

$$\mathbf{Q}_i = \left(\mathbf{\Lambda}_{\mathrm{b}}|_R\right)^{-1} \left(\mathbf{\Phi}_{\mathrm{b}}|_R\right) \mathbf{K}_{\mathrm{b}} \left[\mathbf{\Psi}_{\mathrm{r}} \mathbf{\Phi}_{\mathrm{r}}|_{N\times R}\right]_i \tag{11}$$

where $\mathbf{\Psi}_{\mathrm{r}}$ stands for the transfer matrix between the full finite element space and the reduced space, $\mathbf{\Phi}_{\mathrm{r}}|_{N\times R}$ is the restriction of $\mathbf{\Phi}_{\mathrm{r}}$ to the $N \times R$ first modes and $[\cdot]_i$ refers to the restriction to degrees of freedom of blade i.

2.2 Solution paradigms

Two approaches may be found in the literature to solve Eq. (1): time integration strategies [51] and frequency methods [56, 57]. Time integration methods have been employed to treat contact problems with high relative speeds (such as blade-tip/casing interactions) while frequency methods are usually preferred when dealing with friction and lower relative speeds (such as blade-root/disk interactions). Recently, developments were made to break the silos between these two methodologies: it has been shown that frequency methods such as the Harmonic Balance Method (HBM) can indeed be used for the prediction of blade-tip/casing contacts [50] for a single blade.

On the one hand, time integration methods advantageously allow to compute transient responses and to capture non-periodic responses such as diverging or chaotic motions [58]. It is also well-suited to manage abradable coating wear. However, the computed response is strongly dependent on the selected initial conditions. On the other hand, frequency-based strategies may be able to capture several coexisting solutions thus providing a qualitative view of the system's dynamics. While the assumption of periodicity may be lifted in certain conditions, it is not yet possible to account for abradable coating wear.

2.3 Time domain

Only key equations are recalled in this section since a more detailed presentation of the time integration solution method has already been published [26]. Time integration (TI) methods consist in solving the equation of motion (Eq. (1)) in the time domain for each time step. A central finite difference scheme combined with Lagrange multipliers to manage contacts between the blades tip and the casing is used in this article [51]. At each time step, the displacement vector $\mathbf{u}_{\mathrm{r}}$ is predicted using:

$$\mathbf{u}_{\mathrm{r}}^{p}|_{n+1} = \left(\frac{\mathbf{M}_{\mathrm{r}}}{h^2} + \frac{\mathbf{D}_{\mathrm{r}}}{2h}\right)^{-1} \left[\left(\frac{2\mathbf{M}_{\mathrm{r}}}{h^2} - \mathbf{K}_{\mathrm{r}}\right)\mathbf{u}_{\mathrm{r}}|_n + \left(\frac{\mathbf{D}_{\mathrm{r}}}{2h} - \frac{\mathbf{M}_{\mathrm{r}}}{h^2}\right)\mathbf{u}_{\mathrm{r}}|_{n-1}\right] \tag{12}$$

in which $\mathbf{D}_{\mathrm{r}}$ is the reduced damping matrix and h the time step. If a contact is detected for the predicted displacement, a correction is applied such as:

$$\mathbf{u}_{\mathrm{r}}|_{n+1} = \mathbf{u}_{\mathrm{r}}^{p}|_{n+1} + \left(\frac{\mathbf{M}_{\mathrm{r}}}{h^2} + \frac{\mathbf{D}_{\mathrm{r}}}{2h}\right)^{-1} \boldsymbol{\lambda} \tag{13}$$

where $\boldsymbol{\lambda}$ stands for the contact forces, that can be computed using the predicted interpenetration between the blade and the casing.

2.4 Frequency domain

The Regularized-Lanczos harmonic balance method (RL-HBM) detailed in [50] is used to solve the equation of motion and the contact model in the frequency domain. RL-HBM offers an alternative to the TI strategy for the computation of periodic responses. In this approach, the normal components of contact forces are evaluated as follows:

$$f_{\mathrm{n},j}(t) = \kappa\frac{g_j(t)}{2} + \sqrt{\left(\kappa\frac{g_j(t)}{2}\right)^2 + \gamma^2} \tag{14}$$

where g_j is the gap function that represents the signed distance between contact nodes and the casing at the j-th instant of one revolution, $\kappa \in \mathbb{R}_+$ is a penalty coefficient and $\gamma \in \mathbb{R}_+$ a smoothing parameter. While a classical HBM approach would fail due to the poor convergence behaviour of Fourier series when approximating discontinuous functions—a phenomenon referred to as the Gibbs phenomenon—, RL-HBM relies on a regularization of a bilinear penalty law to increase the numerical robustness of the solver and a Lanczos-filtering of contact forces to mitigate the Gibbs phenomenon:

$$\mathbf{f}_{\mathrm{c}}(\mathbf{u}_{\mathrm{r}}, \dot{\mathbf{u}}_{\mathrm{r}}, \omega) \simeq \frac{1}{2}\mathbf{a}_0^{\mathrm{nl}} + \sum_{j=1}^{H} \sigma_j \left[\mathbf{a}_j^{\mathrm{nl}} \cos(j\omega t) + \mathbf{b}_j^{\mathrm{nl}} \sin(j\omega t)\right] \tag{15}$$

where σ_j are the Lanczos factors, $\mathbf{a}_j^{\mathrm{nl}}$ and $\mathbf{b}_j^{\mathrm{nl}}$ are the nonlinear forces Fourier coefficients, and H is the number of harmonics. The use of a penalty law in this method allows minor penetrations between the blades and the casing, but they remain two to three orders of magnitude smaller than the displacement amplitudes.

3 Rubbing interactions for full bladed disks

As mentioned in the introduction, reported rubbing interactions typically involve a single blade [58]. As a consequence, associated numerical models oftentimes rely on the finite element model of a blade clamped at its root [7]. In this context, this section intends to demonstrate that it is possible—at least from a numerical standpoint—to generate a rubbing interaction using a full bladed disk. To this end, the dynamics of a full industrial bladed disk is analyzed along with that of only one of its blades as they both impact the same deformed casing. To the best authors' knowledge, such single blade versus full bladed disk rubbing interaction comparison has never been addressed before.

3.1 Modelling and interaction point

The bladed disk of interest is the first stage of a low-pressure compressor that counts $N = 21$ blades. The reference sector of the full bladed disk model is shown in Fig. 1a where the blade is colored in light gray (■), the disk sector in dark gray (■) and the cyclic boundaries in orange (■). The bladed disk is clamped at its downstream flange. The single blade model consists in the restriction of the bladed disk to a single blade clamped at its root, see Fig. 1b. Both models rotate around the z-axis and their nominal angular speed is denoted Ω_n.

For both ROM, three boundary nodes (●)—at leading edge (LE), mid-chord (MC) and trailing edge (TE)—are retained along the blade-tip for contact management. The single blade ROM also features 6 fixed-interface modes while the bladed disk ROM includes the first 6 modes for each nodal diameter. The asymptotic convergence of the ROM with respect to the number of modes has been verified but is not detailed here for the sake of conciseness.

The Campbell diagrams of both models are plotted in Fig. 2. Orange (—) and dashed black (----) lines respectively refer to the bladed disk and the blades' eigenfrequencies. Gray lines represent the engine orders (—). The interaction of interest corresponds to the intersection of the first bending mode with the second engine order, which is located at about 70 % of the nominal speed Ω_n. For the full bladed disk, the intersection of the first bending (1B) mode featuring two nodal diameters and engine order (EO) 2 occurs for the angular speed Ω_{i}. Similarly, the intersection between the clamped blade's 1B mode and EO 2 occurs at $\Omega_{\mathrm{i}}^{\mathrm{b}}$, see Fig. 2b.

The nodal diameter map of the bladed disk is shown in Fig. 3. Because the bladed disk counts $N = 21$ blades, the maximum number of nodal diameters is equal to $\lfloor \frac{N}{2} \rfloor = 10$. Orange circles correspond to the bladed disk eigenfrequencies (●), and dashed black lines refer to the clamped blade eigenfrequencies (----). It may be seen that the 1B mode family is clustered due to a high modal density. The bladed disk frequencies related to 1B modes are lower than the clamped blade ones because of the disk flexibility. The 1B mode with 2 nodal diameters is highlighted (○).

3.2 Contact scenario

The contact scenario is defined as follows: at rest, blade-tip/casing clearances are uniform along the casing circumference. During the first 0.04 s of the simulations, the casing is progressively deformed along two angularly opposite locations to initiate contact. The blade-tip/casing clearances at rest is equal to 0.5 mm and the amplitude of

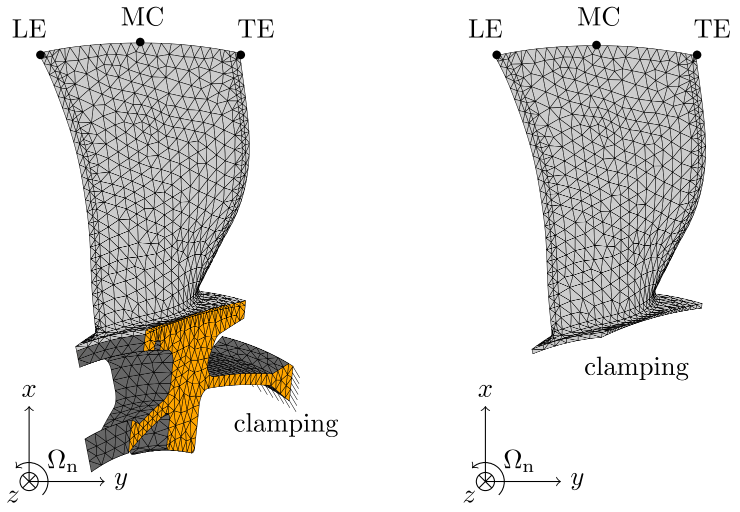

(a) reference sector

(b) clamped blade

Figure 1. finite element models, blade (■), disk sector (■), cyclic boundary (■) and boundary nodes (●)

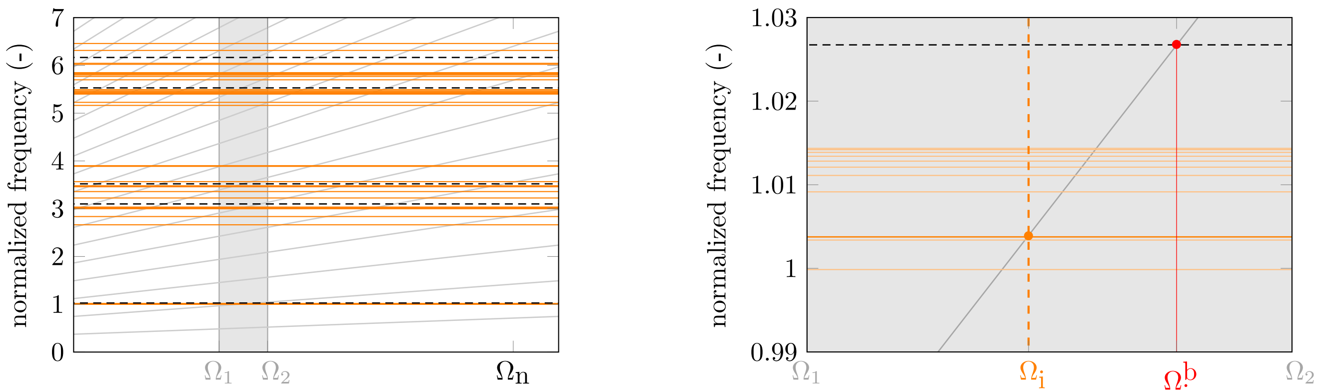

(a)

(b) zoom on the 1B mode family

Figure 2. Campbell diagrams: bladed disk (—), clamped blade (----), engine order lines (—)

the casing deformation is 0.125 mm. A dry friction contact with a Coulomb law is considered between the blade-tip and the casing in the tangential and axial directions, with a friction coefficient μ equals to 0.15. The considered time step h for the resolution of the equation of motion is $h = 10^{-7}$ s. The modal damping coefficients are equal to 0.001 for the three first mode families, and to 0.005 for higher modes. An angular speed range including both Ω_{i} and $\Omega_{\mathrm{i}}^{\mathrm{b}}$ is considered. Simulations are carried out for 100 engine revolutions at constant angular speed. In this section, only the time integration method is considered.

3.3 Frequency response curves

The norm of the maximum radial displacement at the leading edge of the single blade model is shown in Fig. 4b. The same quantity for the bladed disk model is depicted in Fig. 4a. A significant increase of the displacements amplitude is observed after the angular speed $\Omega_{\mathrm{i}}^{\mathrm{b}}$ for the single blade model and after Ω_{i} for the bladed disk model.

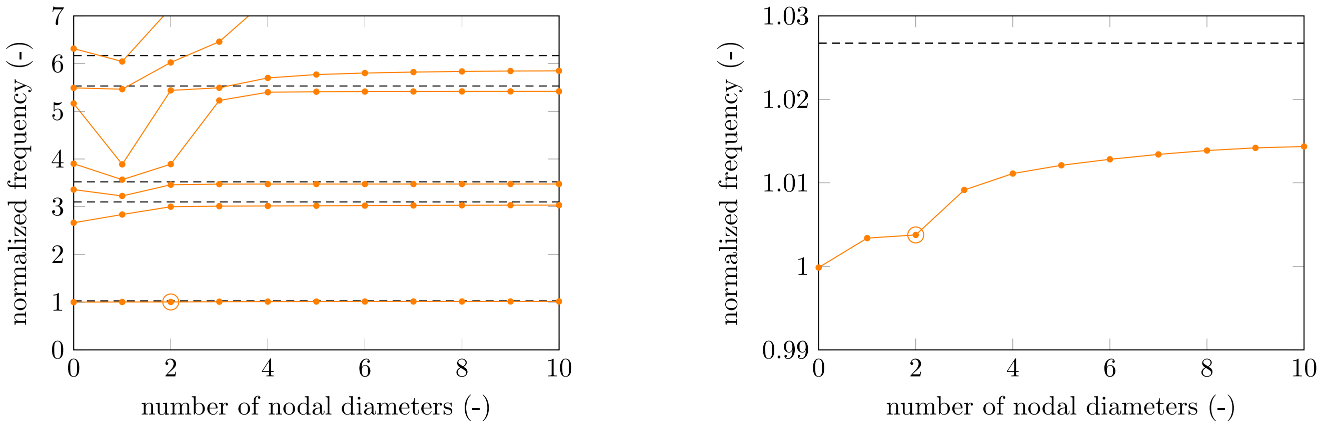

(a)

(b) zoom on the 1B mode family

Figure 3. Nodal diameter map: bladed disk frequencies (●), clamped blade frequencies (----)

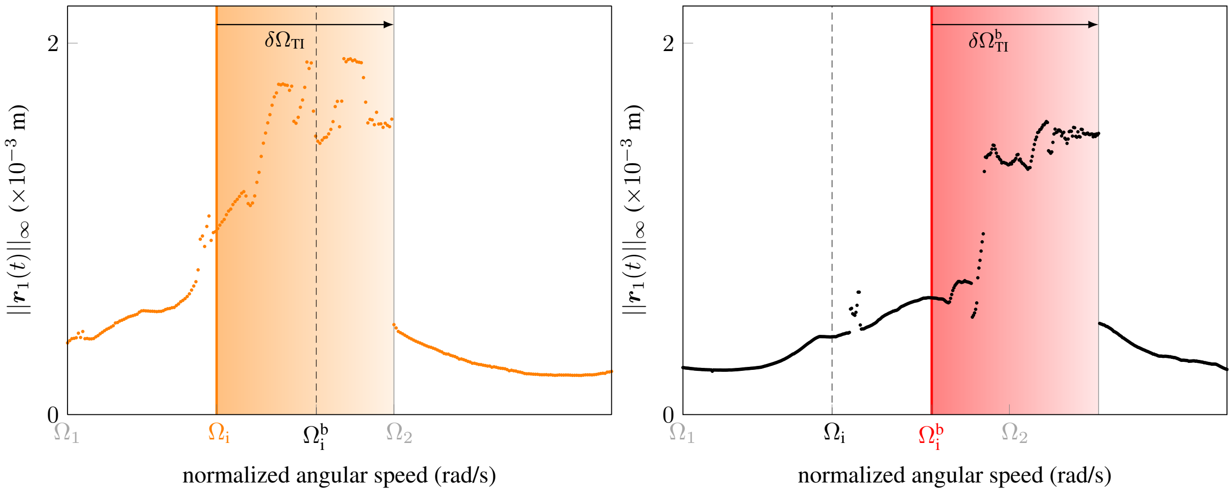

(a) bladed disk model

(b) clamped blade model

Figure 4. norm of the maximum radial displacement at the leading edge of blade 1

In the case of the single blade model, the first bending mode is excited by the engine order 2 excitation. For the full bladed disk, the first bending model with 2 nodal diameters responds. Then, a sudden drop to lower amplitudes occurs when the angular speed further increases. Results suggest a contact stiffening $\delta\Omega_{\mathrm{TI}}^{\mathrm{b}}$ for the single blade model and $\delta\Omega_{\mathrm{TI}}$ for the bladed disk model that both correspond to approximately 4 % of frequency increase.

3.4 Interaction maps

For each angular speed, a Fast Fourier Transform of the time evolution of the radial displacement at the leading edge of blade 1 during the last 50 revolutions is computed. Frequency spectra for each angular speed are put side by side to draw the interaction maps pictured in Fig. 5. White and black colors correspond respectively to low and high amplitudes. In these interaction maps, it is observed that the system's response is located along even engine order lines, which is consistent with the imposed two-lobe symmetric deformation on the casing. Overall, the frequency response curves and the interaction maps both underline that a similar type of vibration response occur

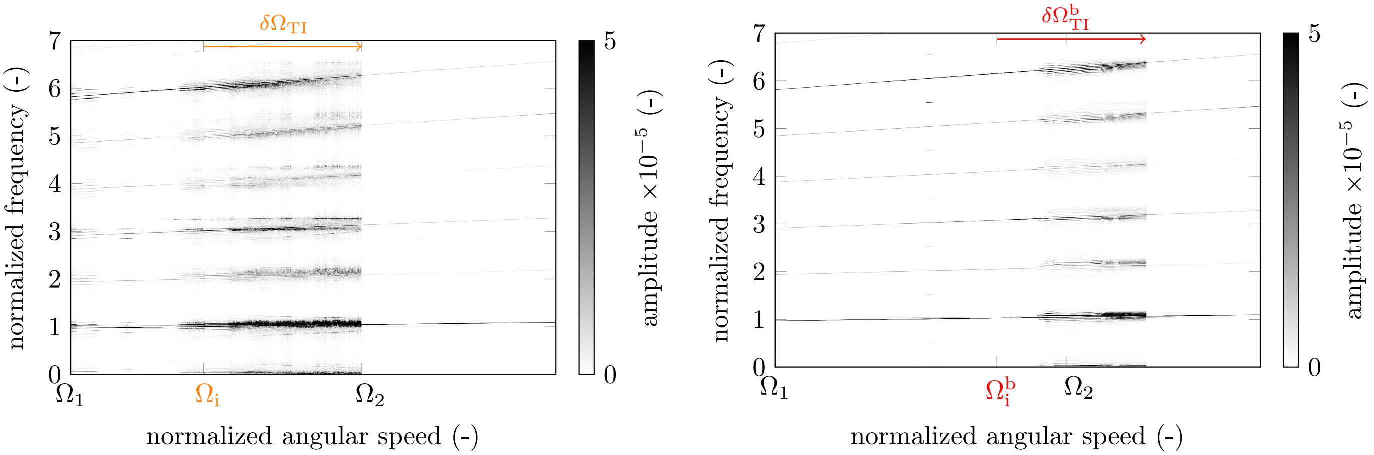

(a) bladed disk model

(b) clamped blade model

Figure 5. interaction maps for the TI strategy for simulations with blade/casing contacts

in the single blade and in the full bladed disk models: vibration amplitudes are of comparable magnitude, contact stiffening is identical and the frequency content is very similar. This is an important observation as it suggests that the predicted interaction on the full bladed disk may be seen as a sum of rubbing interactions occurring at the same time on each of its blades. Thus, the disk dynamics does not play any significant role for this interaction, which is consistent with the fact the 1B modal family is very clustered on the nodal diameter map. Indeed, while this is not shown here for the sake of brevity, it has been observed that the vibration energy of the bladed disk is essentially located in its blades with only a minor participation of the disk.

In the end, the fact that the simulated interaction involves the blades only is also essential in that it makes it suitable for an investigation with respect to mistuning using specific efficient model reduction methods.

4 Definition of a suitable solution paradigm

The investigation of the influence of mistuning in the context of the rubbing interaction identified in the previous section is a challenging task. As explained above, both time and frequency solution methods may be considered. While time integration would unavoidably yield costly simulations, the analysis of mistuned bladed disk ROM featuring a large number of nonlinear degrees of freedom is also extremely demanding and may raise accuracy and efficiency challenges with frequency methods.

Accordingly, the section details the pros and cons of each method for tuned and mistuned ROM. The focus is made on highlighting the limitations inherent to each solution method. To the best of the authors' knowledge, this is the first time that a full bladed disk model undergoing structural contacts along its blade-tips is comparatively analyzed using time and frequency solutions methods. In order to clearly separate the numerical challenges related to the size of the ROM and mistuning itself, a tuned bladed disk is first considered before computations are made for a few mistuned ROM.

4.1 Tuned bladed disk

The norm of the radial displacement at the leading edge of blade 1 obtained using the RL-HBM and TI methods is plotted in Fig. 6. The black curve (——) corresponds to results obtained with the RL-HBM method ($H = 20$ harmonics are considered in the Fourier series and contact forces are evaluated at 1024 instants within time domain), while the orange dots (●) are related to TI results, previously plotted in Fig. 4a. The first obvious observation relates to the fact that a very large portion of the frequency response curve predicted by the RL-HBM is completely

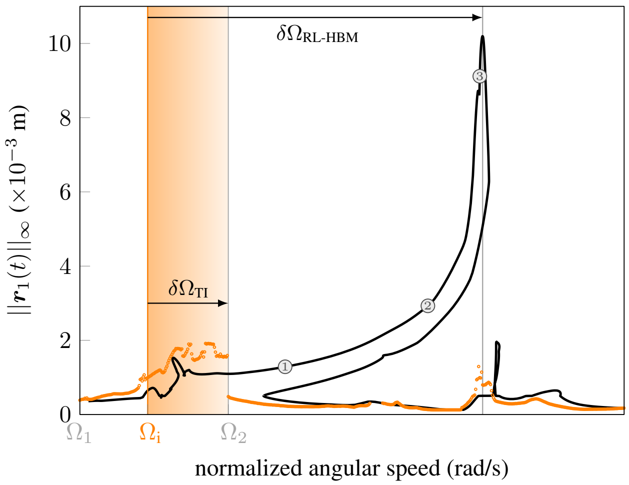

Figure 6. norm of the radial displacement at the leading edge of blade 1 obtained with the RL-HBM method (—) and the TI strategy (●)

absent of the TI results. Areas of discrepancy essentially involve high amplitude solutions while there is a very good superimposition of the results for most low-amplitude solutions. Accordingly, TI and RL-HBM results yield to very distinct predictions in terms of contact stiffening. The 4 % increase of the resonance frequency predicted by TI is dwarfed by the 17 % increase predicted by RL-HBM. Interestingly, this 17 % increase is in line with experimental observations made for blades of similar size [58]. However, one may note that the predicted amplitudes at the nonlinear resonance by the RL-HBM must be put in perspective as a 10 mm radial displacement makes no physical sense for the considered bladed disk. Past a certain threshold—which is located in the vicinity of about 4 mm in this case—predicted results become incompatible with the assumption of small deformations inherent to the employed linear finite element models.

Because the TI results do not provide any point on most of the higher amplitude branch of results predicted by RL-HBM, it is essential to ensure that these solutions are not numerical artefacts. To this end, three points on this branch, denoted ①, ② and ③ in Fig. 6, have been selected and used as initial conditions of the TI solver. The obtained TI results are compared with the RL-HBM ones in Figs. 7, 8 and 9 over one period. Radial displacements, contact forces as well as velocities at the leading edge of each blade are almost perfectly superimposed. This is proof that the three selected points may be obtained using the TI strategy using different initial conditions. Also, as expected for the tuned bladed disk, a phase shift of $\frac{2\pi}{N}$ is observed between the signals of two adjacent blades.

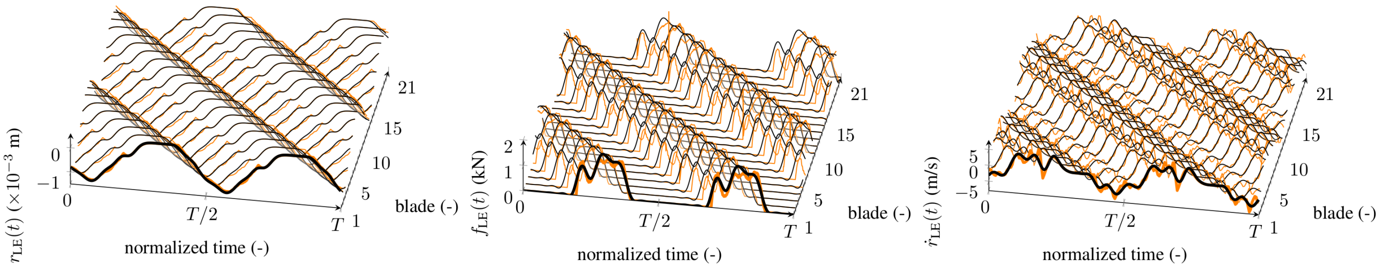

(a) displacement **(b)** contact force **(c)** velocity

Figure 7. TI (—) and RL-HBM (—) solution at the LE of each blade in the radial direction for point ①

In the end, the presented results underline the consistence both TI and RL-HBM for the analysis of a tuned bladed disk undergoing structural contacts along its blade-tips. It also emphasizes the ability of the RL-HBM to

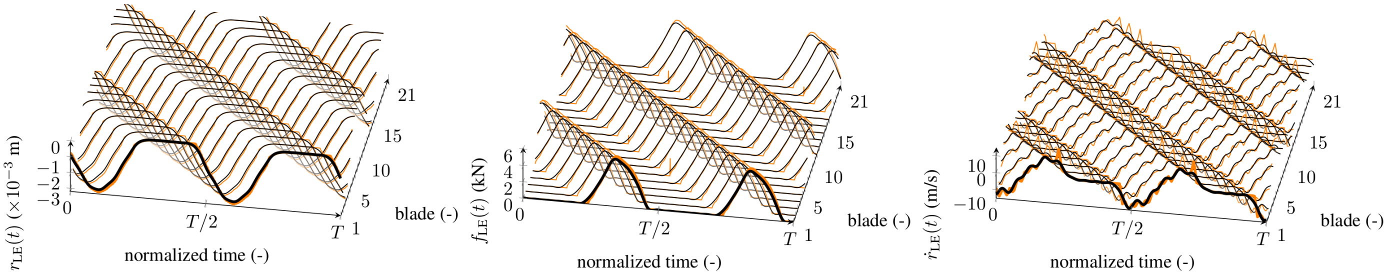

(a) displacement **(b)** contact force **(c)** velocity

Figure 8. TI (—) and RL-HBM (—) solution at the LE of each blade in the radial direction for point ②

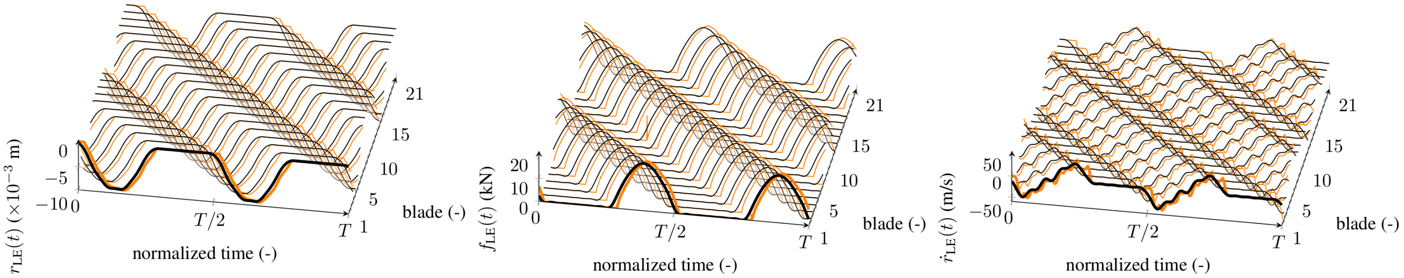

(a) displacement **(b)** contact force **(c)** velocity

Figure 9. TI (—) and RL-HBM (—) solution at the LE of each blade in the radial direction for point ③

deal with large nonlinear systems since the tuned bladed disks features 9 nonlinear degrees of freedom per blade, meaning a total of 189 nonlinear degrees of freedom. For the tuned bladed disk, as previously evidenced on single blade models [50], the RL-HBM has a key advantage over TI since it is capable of capturing the actual nonlinear resonance of the system. The latter is indeed significantly underestimated by TI.

4.2 Mistuned bladed disk

Mistuning is introduced in the bladed disk ROM using the methodology presented in section 2.1.2. The comparison between TI and RL-HBM solutions in the mistuned case is assessed on three mistuning samples. These randomly selected samples are detailed in Fig. 10. Each sample feature a distinct degree of mistuning: 1 % (■), 2 % (■), and 3 % (■) are considered.

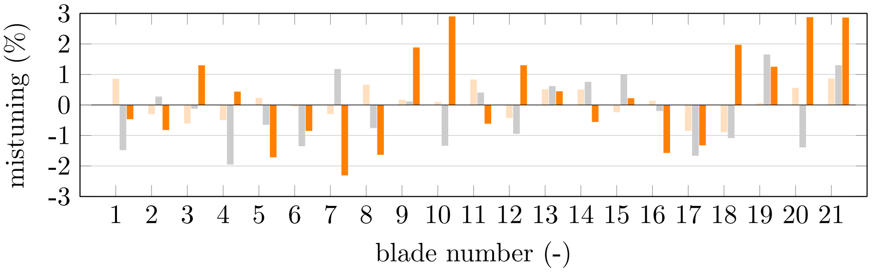

Figure 10. mistuning patterns: 1 % (■), 2 % (■) and 3 % (■)

The amplitude at the leading edge of blade 1 obtained using the RL-HBM method (—) and the TI strategy (●) are superimposed in Fig. 11. For each mistuning pattern, TI results are comparable to those obtained in the tuned case: a steady increase of the vibration amplitudes is predicted passed the interaction speed Ω_i. Passed a certain

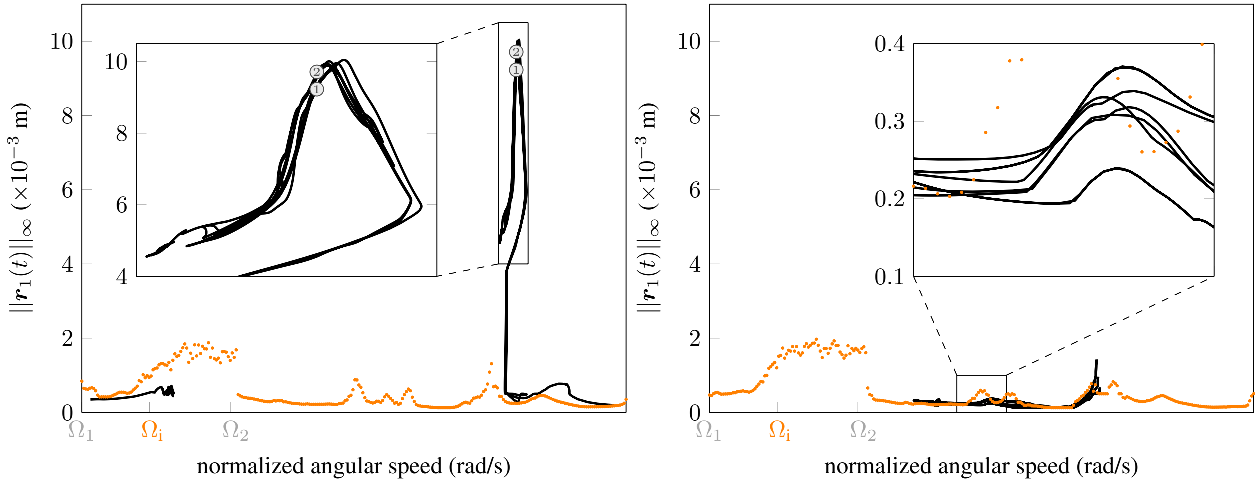

(a) 1 %

(b) 2 %

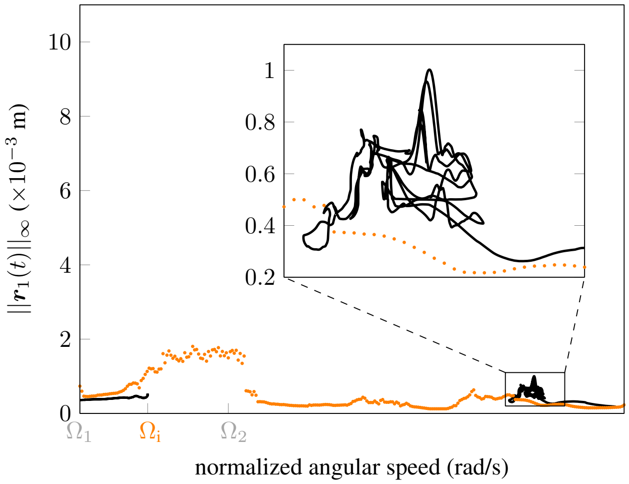

(c) 3 %

Figure 11. norm of the radial displacement at the leading edge of blade 1 for simulations with blade/casing contacts and the selected mistuning patterns obtained with the RL-HBM method (——) and TI strategy (●)

point, amplitudes of vibration suddenly decrease and minor peaks of amplitude are predicted throughout the rest of the angular speed range. With the RL-HBM however, only portions of the frequency response curves could be obtained due to cumbersome computation times and an extreme numerical sensitivity of the solver in specific areas such as turning points.

Where results could be obtained with the RL-HBM, frequency response curves exhibit a remarkably complex dynamics with a very large number of coexisting solutions at each angular speed. In order to assess the validity of these numerical predictions, two points, see ① and ② in Fig. 11a, have been randomly chosen, at the same angular speed, for a degree of mistuning of 1 % in the vicinity of the predicted nonlinear resonance to define initial conditions for the TI method. The superimposition of TI and RL-HBM results over a full period is depicted in Figs. 12 and 13.

It is observed that there is an excellent match between TI and RL-HBM results, in terms of displacements, contact forces and velocities. This indicates that, despite of the numerical sensitivity of the RL-HBM, the predicted solutions are indeed numerically relevant and very precise: it is indeed possible to capture the dynamics of a mistuned bladed

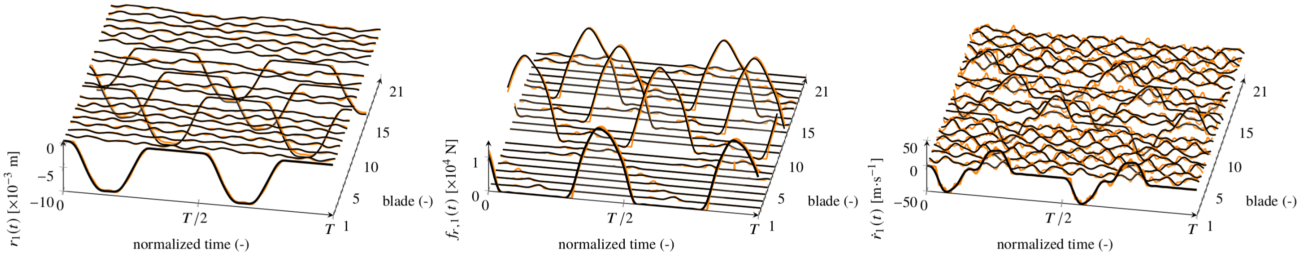

(a) displacement **(b)** contact force **(c)** velocity

Figure 12. TI (—) and RL-HBM (—) solutions at the LE of each blade in the radial direction at point ①

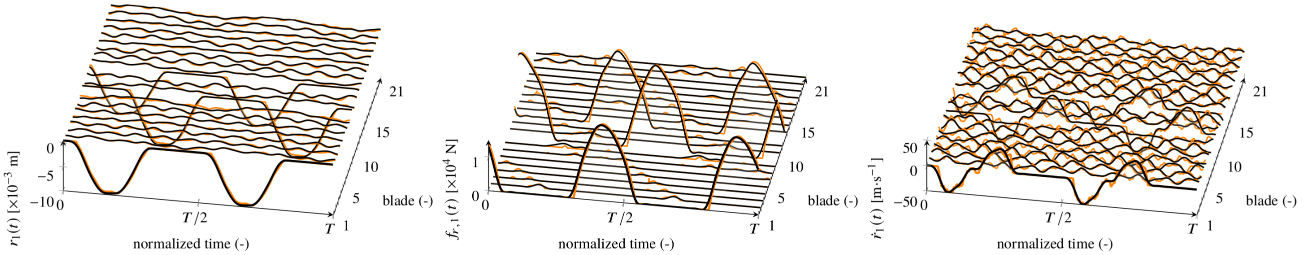

(a) displacement **(b)** contact force **(c)** velocity

Figure 13. TI (—) and RL-HBM (—) solutions at the LE of each blade in the radial direction at point ②

disk with a very low degree of mistuning. Nonetheless, contrary to what was observed in the previous section, the RL-HBM cannot yet be used for an efficient prediction of a mistuned bladed disk nonlinear resonance. In addition, could the issue of numerical sensitivity be overcome, the extraordinary complexity of the system's dynamics would still yield unacceptably long computation times in the context of a stochastic analysis.

In the end, it is evidenced that the considered time and frequency solution methods are not suitable for an accurate prediction of a mistuned bladed-disk nonlinear resonance in the context of blade-tip/casing structural contacts. This constitutes a fundamental roadblock for a comprehensive investigation of the influence of mistuning combined with nonlinear structural interactions in terms of amplification factor. For all these reasons, in the remainder, the focus is made on the localization factor and the TI method is the only one considered for the stochastic analysis in a bladed disk/casing interaction accounting for abradable wear.

5 Influence of mistuning for bladed disk/abradable contacts

An abradable coating is frequently deposited along the casing contact surface in order to prevent significant damage on the blades when blade-tip/casing contacts occur. In addition to the numerical difficulties mentioned in the previous section, accounting for abradable coating removal—because of the required update of the blade-tip/casing clearance configuration it implies—is currently another roadblock for considering frequency methods for the stochastic analysis carried out in this section. Accordingly, the TI solution method is used in this section.

5.1 Reference configuration: tuned bladed disk

In this section, the interaction point remains related to the intersection of EO 2 with the 1B mode featuring 2 nodal diameters. Contrary to the results presented in section 3.3, abradable coating wear is accounted for. The 5 mm thick abradable layer is considered, with a Young's modulus of 1 GPa, a plastic modulus of 0.25 GPa and a Yield stress of 1.5 MPa.

The frequency response curve for the leading edge of blade 1 of the bladed disk is plotted in Fig. 14. Results are superimposed with those obtained without abradable coating previously shown in Fig. 4a. Similarly to what was

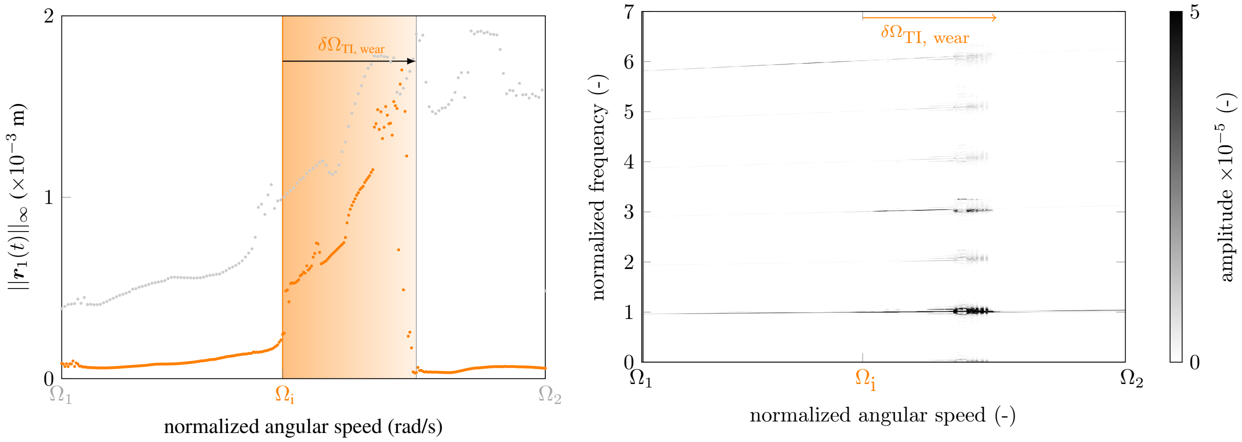

(a) frequency response curve: with (●) and without (●) abradable coating

(b) interaction map

Figure 14. radial displacement at the leading edge of blade 1

observed without abradable coating, the amplitude of vibrations steadily increases passed Ω_i up to a point where a sudden decrease of amplitudes is observed. The corresponding contact stiffening is denoted $\delta\Omega_{\text{TI, wear}}$, it corresponds to about 2 % of the bladed disk eigenfrequency. While amplitudes of vibration are overall significantly reduced when considering an abradable coating, it is remarkable that TI results lead to very close maximum amplitudes of vibration for configurations with and without coating.

In order to get a better understanding of the bladed disk dynamics, the frequency content of its response is pictured in the interaction map 14b. Highest amplitudes of vibration correspond to the darker areas, which are located along even engine orders, mostly the second one. In comparison to the interaction map obtained without abradable coating pictured in Fig. 5a, contributions over higher engine orders are overall significantly reduced. This is consistent with the softer contact configuration induced by the abradable coating.

Finally, wear profiles predicted within the casing abradable coating in front of the blade's leading edge are depicted in Fig. 15. Passed the critical speed Ω_i, two wear lobes are visible—indicated by darker areas. These lobes get deeper as the angular speed increases, see zone 1. A sudden transition is observed (from zone 1 to zone 2) where the circumferential location of the lobes shifts, thus indicating a change in the nature of the blade's response, also

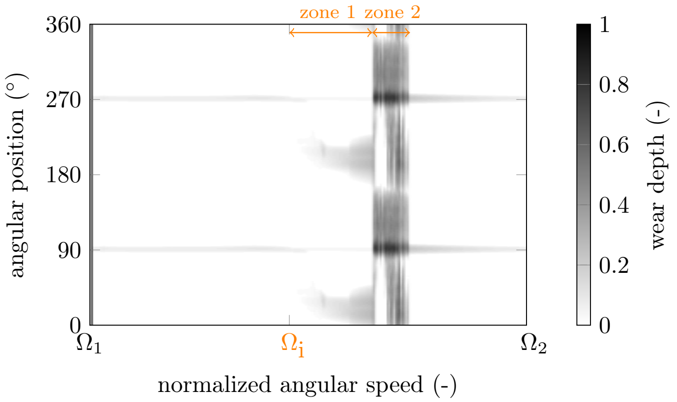

Figure 15. wear map

evidenced by the higher amplitudes of vibration in Fig. 14.

5.2 Stochastic analysis

For the same rubbing configuration as the one presented in the previous section, the ROM of the bladed disk now features a degree of mistuning ranging from $dE = 1$ % to $dE = 3$ %. For each degree of mistuning dE, 1000 samples are drawn considering a uniform distribution $[-dE, dE]$.

5.2.1 Reference point: linear results

The influence of mistuning is first briefly assessed in the context of a linear excitation, considering a two-nodal diameter forcing on the blades. The results presented in this section will serve as a reference point for the nonlinear analysis carried out in the following sections. Two typical quantities of interest are investigated [32, 33, 34, 35]:

the amplification factor (AF): defined as the ratio between the maximum radial displacement of all boundary nodes in the mistuned case and in the tuned case over the angular speed range of interest;

the localization factor (LF): defined as [37]:

$$LF = 100 \times \frac{\zeta - 1}{\sqrt{N} - 1} \qquad \text{with} \qquad \zeta = \frac{\max(\mathbf{U}_{\max})}{\sqrt{\langle \mathbf{U}^2_{\max} \rangle}} \tag{16}$$

where $\mathbf{U}_{\max}$ denotes the maximum radial displacement at the blade-tips for the last engine revolution and $\sqrt{\langle \mathbf{U}^2_{\max} \rangle}$ is the quadratic mean value of $\mathbf{U}_{\max}$. A localization factor of 0 % corresponds to a uniform distribution of the vibrations within all blades, while a value of 100 % corresponds to the case where one blade only vibrates.

The 90th percentile of the maximum radial displacement for all samples over the angular speed range of interest is drawn in Fig. 16 for a degree of mistuning of 1 % (—) and 3 % (—). The tuned response is superimposed in black (—), it features a resonance peak at Ω_i, in agreement with the interaction condition presented in Fig. 2b. The angular speed range featuring high amplitudes of vibration is significantly wider [■, ▲] for $dE = 1$ % and [■, ▲] for $dE = 3$ % than in the tuned case. The boundaries of these ranges, ■ and ▲, are defined using the maximum localization factor values detailed hereafter.

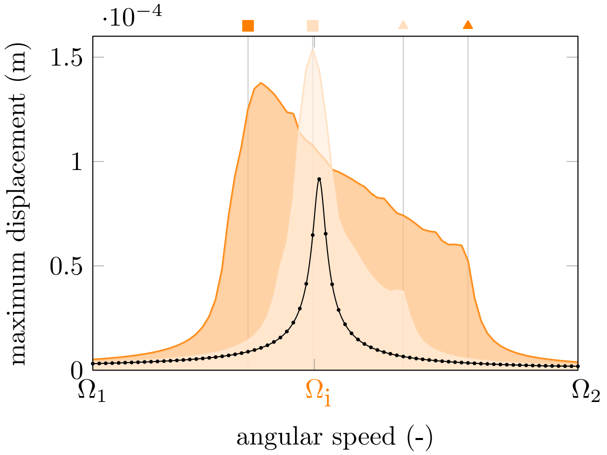

Figure 16. linear forcing: 90th percentile of the maximum displacement: tuned (—), $dE = 1$ % (—) and $dE = 3$ % (—)

The 90th percentile of LF values for all samples is depicted in Fig. 17a for $dE = 1$ % (—) and $dE = 3$ % (—). It is noticeable that maximum values of LF are overall increased as the degree of mistuning is increased. Also, and contrary to what was observed for the amplitudes of vibration, peak values of LF are located at the two edges of an angular speed range that gets wider as dE increases. These peak values are marked with the ■ and ▲ symbols.

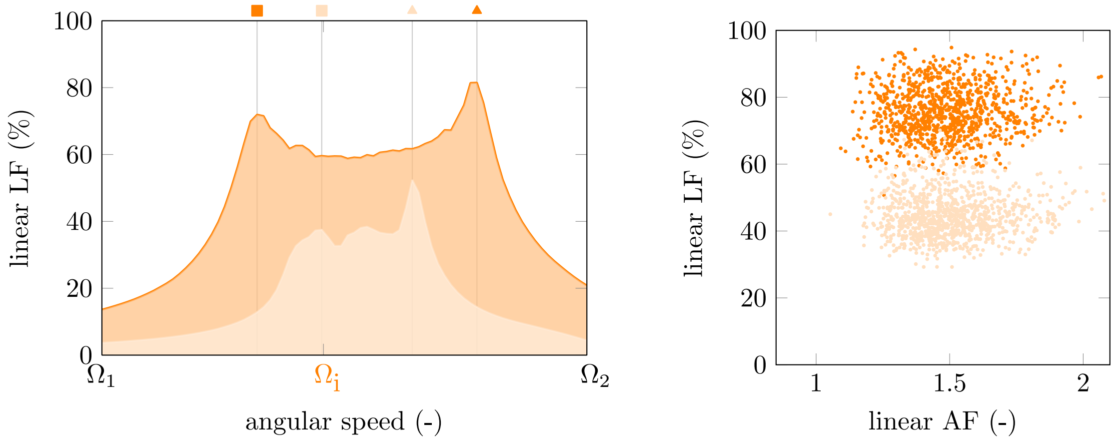

(a)

(b)

Figure 17. linear forcing: 90th percentile of the maximum LF (a), and AF versus maximum LF (b) for $dE = 1$ % (●) and $dE = 3$ % (●)

Finally, an overview of all AF and LF values is plotted in Fig. 17b. AF between 1 and 2.1 are obtained, which is in line with literature values in a linear context [28]. It is observed that AF are not significantly affected by the mistuning level. However, LF values approximately double as the degree of mistuning increases from 1 % to 3 %.

5.2.2 Convergence of the nonlinear simulations

Nonlinear simulations featuring blade-tips/abradable coating contacts are run over 250 revolutions. While it is not detailed here for the sake of brevity, an auto-correlation procedure has been implemented to assess the steadiness of the blade response for each simulation.

As mentioned above, the TI solution method is ill-suited for analyzing AF values. It has indeed been underlined in section 4.1 that TI results most certainly miss the peak of amplitude at the nonlinear resonance. For that reason, the focus is made on ensuring that convergence of the stochastic analysis has been reached for the LF values only. LF values are computed for each sample. The convergence of 10th (—), 50th (—) and 90th (—) percentiles of the nonlinear LF with respect to the number of samples is given in Fig. 18. It is observed that the convergence of the LF values is reached quite quickly as LF values remain very stable once 500 samples have been computed. In

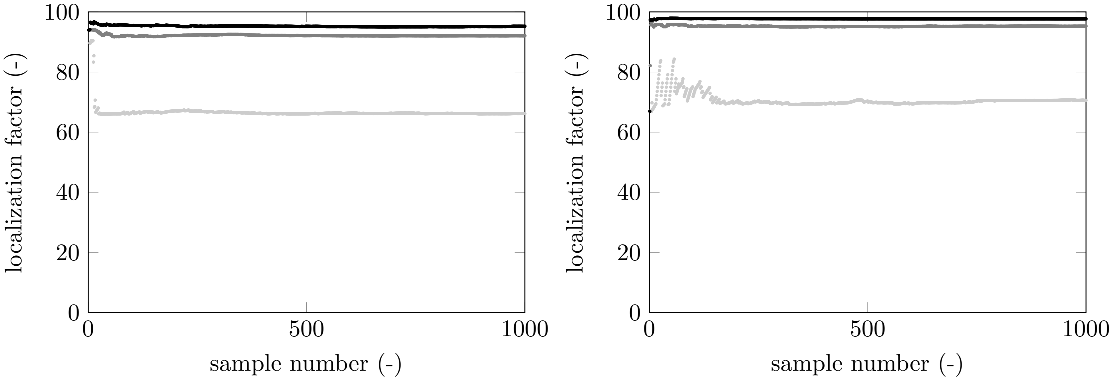

(a) 1 %

(b) 3 %

Figure 18. convergence of the 10th (—), 50th (—) and 90th (—) percentiles of LF with the number of samples

the following, all presented results are obtained with 1000 samples so that results are assumed to be stochastically relevant.

5.2.3 Preliminary remarks on the amplification factors

While aforementioned observations underlined that AF values may not be correctly captured with the employed methodology, the computed AF values were also found to be stochastically converged for 1000 samples. This is unexpected as it was assumed that accounting for mistuning may occasionally allow the time integrator to go further on the branch of solution featuring high amplitudes of vibration, that would have unavoidably impacted AF values. It thus appears that AF values are consistently underestimated with the proposed methodology. This is evidenced in Fig. 19 where the 90th percentile of the maximum radial displacement for all samples is plotted, see Fig. 19a, beside of the comparison of linear and nonlinear AF values, see Fig. 19b. The lack of correlation between linear nonlinear AF values is also consistent with previous results on a phenomenological model [48] and on the same industrial bladed disk [49].

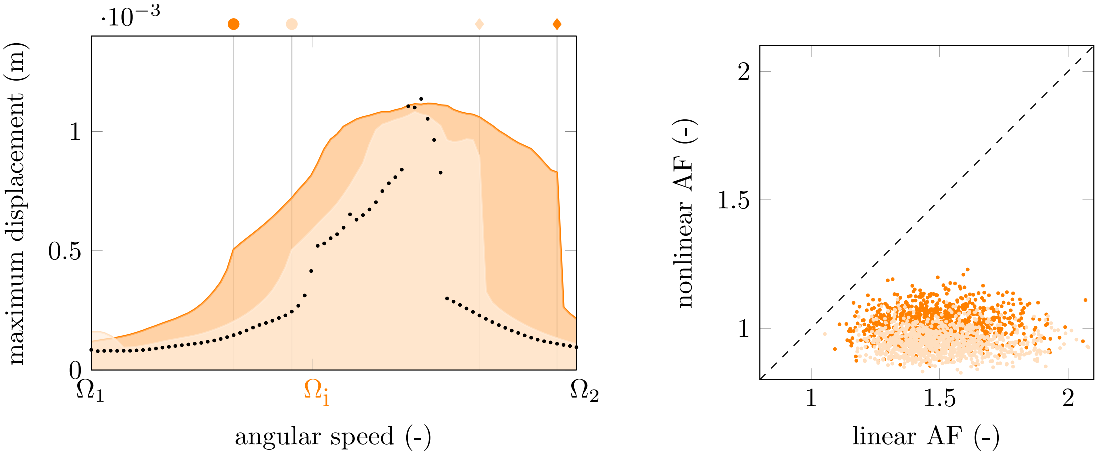

(a) 90th percentile of the maximum displacement

(b) linear versus nonlinear AF

Figure 19. displacements and AF values for the tuned case (•), $dE = 1$ % (—) and $dE = 3$ % (—)

5.2.4 Analysis

First of all, in order to better visualize the meaning of LF values, the radial displacements at the leading edge of each blade is represented for two contact simulations in Fig. 20. In the first case, see Fig. 20a, LF=67 % and it is noticeable that amplitudes of vibration are essentially located on blades 1 and 2. In the second case however, see Fig. 20b, where LF=97 %, only one blade features significant amplitudes of vibration. These two examples underline the relevance of the considered localization factor.

The 90th percentile of LF values over the considered angular speed range for $dE = 1$ % and $dE = 3$ % are depicted in Fig. 21a. Contrary to what was observed in a linear context, see Fig. 17a, the maximum value of LF is close to 100 % no matter the degree of mistuning. In a nonlinear structural context, a significantly more contrasted variation of LF values is predicted. Indeed, LF values are significantly lower than in a linear context between the two peak values. In this area, for $dE = 1$ % and $dE = 3$ %, minimum LF values get respectively close to 0 % and 20 %, far below their respective minimum of 30 % and 60 % in a linear context.

For each sample, the maximum LF value in both linear and nonlinear simulations is displayed in Fig. 21b. There are two aspects underlined by this graphic representation. First of all, nonlinear LF values are, overall, significantly higher than their linear counterparts. Secondly, data points are clustered in two distinct areas: a low nonlinear LF value range around 65 % and a high nonlinear LF value range around 95 %.

In order to understand the origin of this clustering of nonlinear LF values, another visualization is proposed in Fig. 22. In the latter, LF values are plotted using a color code on the frequency response curve of all samples.

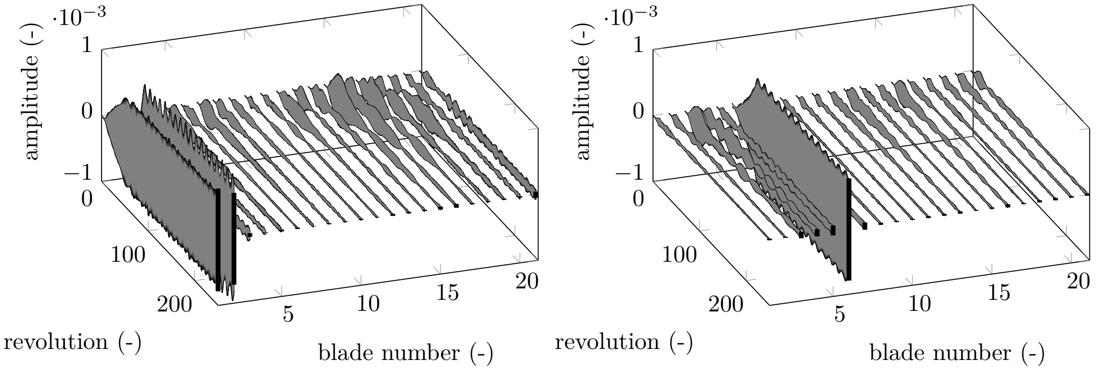

(a) **(b)**

Figure 20. radial displacement at the leading edge of all blades for a simulation with a LF of (a) 67 % and (b) 97 %

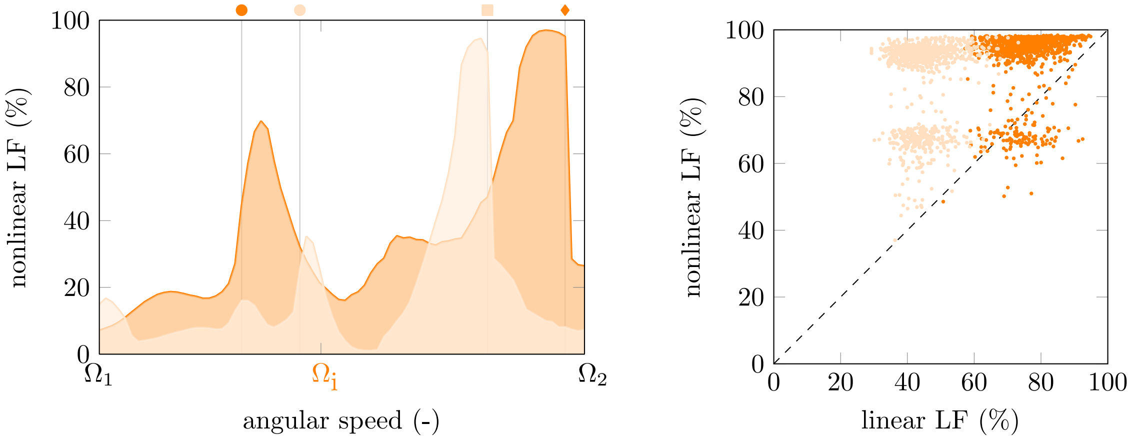

(a) 90th percentile of the maximum LF **(b)** linear versus nonlinear maximum LF

Figure 21. analysis of LF values for $dE = 1$ % (—) and $dE = 3$ % (—)

In agreement with the clustering observed in Fig. 21b, a higher density of frequency response curves is visible for both values of dE around 65 % and 95 %. For all these frequency response curves, maximum LF values are located at the tip of the high amplitude solution branch. A close inspection of these plots also allows to see that these solution branches are slightly longer for samples featuring LF values around 95 %. This is where peak nonlinear LF values are reached. In other words, it appears that continuing along these high amplitude solution branches would yield an extreme localization of the bladed disk response. This may be difficult to capture with the employed TI solution method and could shed a light and why the frequency response curves all feature a jump from high to low amplitudes of vibration in a very narrow angular speed range.

Highly localized solutions featuring high amplitudes of vibration is also consistent with the RL-HBM results presented in Figs. 11a, 12 and 13. In the end, the presented numerical results underline that in a nonlinear context, mistuning may lead to significantly more localized vibration responses. This indicates that rubbing interactions on full bladed disks may be even more detrimental to a bladed disk lifespan than it is to a single blade.

6 Conclusion

This work focuses on the combined analysis of mistuning and blade-tip/abradable coating contacts, more commonly referred to as rubbing interactions, with an industrial bladed disk. It is first numerically evidenced that rubbing

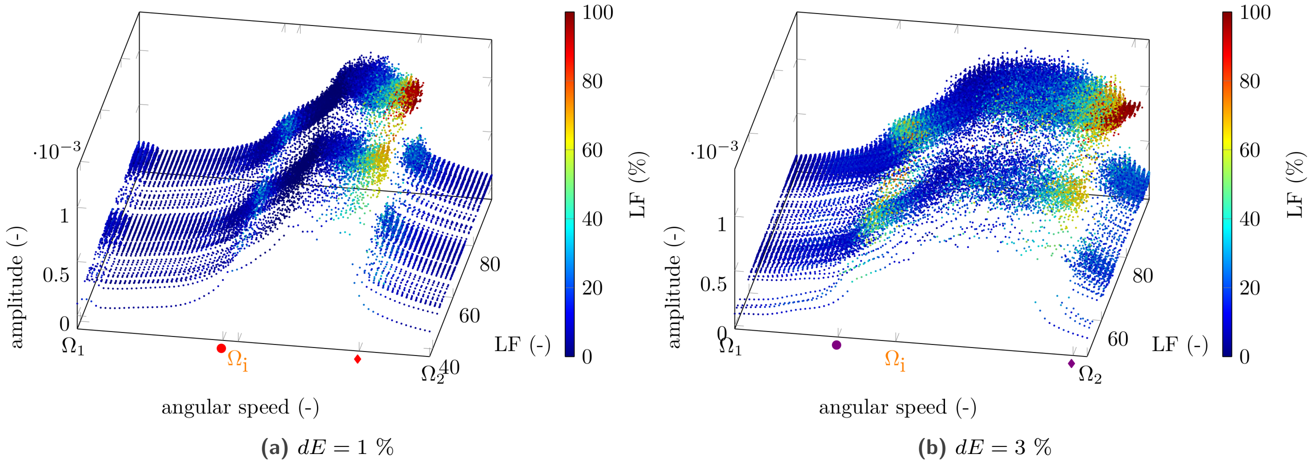

(a) $dE = 1$ % **(b)** $dE = 3$ %

Figure 22. LF values for each simulation, samples are sorted depending on the maximal LF value

interactions may indeed occur on a full bladed disk, thus expanding the notion of rubbing interaction to full bladed disks. Such interaction is characterized by high amplitude of vibrations on all blades and a concentration of the vibration energy on blades only. In that sense, this interaction is thus suitable for a combined analysis with bladed disk mistuning using efficient numerical methodologies assuming material discrepancies are localized on the blades only.

Particular attention is paid to justifying the solution method that is the most suitable for carrying out such numerical investigation. Both frequency and time methods are thoroughly compared. For the first time, a frequency method is shown to accurately predict the vibration response of a full tuned bladed disk undergoing structural blade-tip/casing contacts. There is an excellent agreement between time and frequency solution methods but it is also emphasized that time solution methods seem ill-suited to capture the system's nonlinear resonance. When considering mistuning however, the extreme intricacy of the system's dynamics makes the employed frequency method unable to capture a full frequency response curve within reasonable computation times. Because of these numerical challenges, and because abradable coating wear modelling is only possible using time integration, the latter is used to carry out a stochastic analysis on the influence of mistuning on a full bladed disk's response in the context of rubbing interactions.

An in-depth analysis of the stochastic results reveals the significant increase of localization factors in a nonlinear context. In total, 1000 samples are used with two distinct degrees of mistuning (1 % and 3 %). Because of current limitations in terms of solution methods, presented results cannot yet be analyzed in terms of amplification factors. This will require further numerical developments as significant roadblocks must be lifted both in time and frequency domains.

Acknowledgment

This research was supported by the Natural Sciences and Engineering Research Council of Canada (NSERC) (grant number RGPIN-2016-06390) and the Canada Research Chairs Program (Funder ID: 10.13039/501100000038).

References

[1] Vernet, N., Ruiz, E., Advani, S., Alms, J., Aubert, M., Barburski, M., Barari, B., Beraud, J., Berg, D., Correia, N., Danzi, M., Delaviere, T., Dickert, M., Fratta, C. D., Endruweit, A., Ermanni, P., Francucci, G., Garcia, J., George, A., Hahn, C., Klunker, F., Lomov, S., Long, A., Louis, B., Maldonado, J., Meier, R., Michaud, V., Perrin, H., Pillai, K., Rodriguez, E., Trochu, F., Verheyden, S., Wietgrefe, M., Xiong, W., Zaremba, S., and

Ziegmann, G., 2014. “Experimental determination of the permeability of engineering textiles: benchmark II”. *Composites Part A,* **61**, pp. 172–184. doi: 10.1016/j.compositesa.2014.02.010.

[2] Nyssen, F., Tableau, N., Lavazec, D., and Batailly, A., 2020. “Experimental and numerical characterization of a ceramic matrix composite shroud segment under impact loading”. *Journal of Sound and Vibration,* **467**, p. 115040. doi: 10.1115/1.4033065 - oai: hal-02378746v1.

[3] Padova, C., Barton, J., Dunn, M., and Manwaring, S., 2006. “Experimental results from controlled blade tip/shroud rubs at engine speed”. *Journal of Turbomachinery,* **129**(4), pp. 713–723. doi: 10.1115/1.2720869.

[4] Batailly, A., Legrand, M., Millecamps, A., and Garcin, F., 2012. “Numerical-experimental comparison in the simulation of rotor/stator interaction through blade-tip/abradable coating contact”. *Journal of Engineering for Gas Turbines and Power,* **134**(8), August, p. 11. doi: 10.1115/1.4006446 - oai: hal-00746632.

[5] Almeida, P., Gibert, C., Thouverez, F., Leblanc, X., and Ousty, J., 2016. “Numerical analysis of bladed disk-casing contact with friction and wear”. *Journal of Engineering for Gas Turbines and Power,* **138**(12), p. 11. doi: 10.1115/1.4033065.

[6] Turner, K. E., Dunn, M., and Padova, C., 2010. “Airfoil Deflection Characteristics During Rub Events”. American Society of Mechanical Engineers Digital Collection, pp. 779–789. doi: 10.1115/GT2010-22166.

[7] Batailly, A., Agrapart, Q., Millecamps, A., and Brunel, J.-F., 2016. “Experimental and numerical simulation of a rotor/stator interaction event localized on a single blade within an industrial high-pressure compressor”. *Journal of Sound and Vibration,* **375**, August, pp. 308–331. doi: 10.1016/j.jsv.2016.03.016 - oai: hal-01342401.

[8] Schmiechen, P., 1997. “Travelling Wave Speed Coincidence”. PhD thesis. available online.

[9] Legrand, M., Pierre, C., Cartraud, P., and Lombard, J.-P., 2009. “Two-dimensional modeling of an aircraft engine structural bladed disk-casing modal interaction”. *Journal of Sound and Vibration,* **319**(1), Jan., pp. 366–391. doi: 10.1016/j.jsv.2008.06.019 - oai: hal-00328186.

[10] Salvat, N., 2005. “Modeling of shaft precessional motions induced by unilateral and frictional blade/casing contacts in aircraft engines”. PhD thesis. oai: tel-01259136.

[11] Williams, R. J., 2012. “Simulation of Blade Casing Interaction Phenomena in Gas Turbines Resulting From Heavy Tip Rubs Using an Implicit Time Marching Method”. American Society of Mechanical Engineers Digital Collection, pp. 1007–1016. doi: 10.1115/GT2011-45495.

[12] Shiembob, L. T., 1975. Continued development of abradable gas path seals. [for gas turbine engines]. Tech. rep. available online.

[13] Yi, M., He, J., Huang, B., and Zhou, H., 1999. “Friction and wear behaviour and abradability of abradable seal coating”. *Wear,* **231**(1), pp. 47–53. doi: 10.1016/S0043-1648(99)00093-9.

[14] Laverty, W. F., 1982. “Rub energetics of compressor blade tip seals”. *Wear,* **75**(1), Jan., pp. 1–20. doi: 10.1016/0043-1648(82)90137-5.

[15] Zhang, B., and Marshall, M., 2019. “Investigating material removal mechanism of Al-Si base abradable coating in labyrinth seal system”. *Wear,* **426-427**, Apr., pp. 239–249. doi: 10.1016/j.wear.2019.01.034.

[16] Dadouche, A., Conlon, M. J., Dmochowski, W., Liko, B., and Bedard, J.-P., 2009. “Experimental Evaluation of Abradable Seal Performance at High Temperature”. American Society of Mechanical Engineers Digital Collection, pp. 143–150. doi: 10.1115/GT2008-51228.

[17] Martinet, B., Cappella, A., Philippon, S., and Montebello, C., 2020. “Effect of temperature on wear mechanisms of an aluminium - based abradable coating for aircraft engines after a dynamic interaction with a Ti6Al4V blade”. *Wear,* **446-447**, Apr., p. 203202. doi: 10.1016/j.wear.2020.203202.

[18] Novinski, E., Harrington, J., and Klein, J., 1982. “Modified zirconia abradable seal coating for high temperature gas turbine applications”. *Thin Solid Films,* **95**(3), Sept., pp. 255–263. doi: 10.1016/0040-6090(82)90018-9.

[19] Padova, C., Dunn, M. G., Barton, J., Turner, K., Turner, A., and DiTommaso, D., 2011. "Casing Treatment and Blade-Tip Configuration Effects on Controlled Gas Turbine Blade Tip/Shroud Rubs at Engine Conditions". *Journal of Turbomachinery,* **133**(1), Jan. doi: 10.1115/1.4000539.

[20] Cuny, M., Philippon, S., Chevrier, P., and Garcin, F., 2014. "Experimental Measurement of Dynamic Forces Generated during Short-Duration Contacts: Application to Blade-Casing Interactions in Aircraft Engines". *Experimental Mechanics,* **54**(2), Feb., pp. 101–114. doi: 10.1007/s11340-013-9780-z.

[21] Mandard, R., Witz, J.-F., Boidin, X., Fabis, J., Desplanques, Y., and Meriaux, J., 2015. "Interacting force estimation during blade/seal rubs". *Tribology International,* **82**, Feb., pp. 504–513. doi: 10.1016/j.triboint.2014.01.026.

[22] Nitschke, S., Wollmann, T., Ebert, C., Behnisch, T., Langkamp, A., Lang, T., Johann, E., and Gude, M., 2019. "An advanced experimental method and test rig concept for investigating the dynamic blade-tip/casing interactions under engine-like mechanical conditions". *Wear,* **422-423**, Mar., pp. 161–166. doi: 10.1016/j.wear.2018.12.072.

[23] Sinha, S. K., 2005. "Non-linear dynamic response of a rotating radial Timoshenko beam with periodic pulse loading at the free-end". *International Journal of Non-Linear Mechanics,* **40**(1), Jan., pp. 113–149. doi: 10.1016/j.ijnonlinmec.2004.05.019.

[24] Parent, M.-O., Thouverez, F., and Chevillot, F., 2014. "Whole Engine Interaction in a Bladed Rotor-to-Stator Contact". American Society of Mechanical Engineers Digital Collection. doi: 10.1115/GT2014-25253.

[25] Guérin, N., Thorin, A., Thouverez, F., Legrand, M., and Almeida, P., 2019. "Thermomechanical Model Reduction for Efficient Simulations of Rotor-Stator Contact Interaction". *Journal of Engineering for Gas Turbines and Power,* **141**(2), Feb. doi: 10.1115/1.4040858 - oai: hal-01713849.

[26] Legrand, M., and Pierre, C., 2010. "Numerical Investigation of Abradable Coating Wear Through Plastic Constitutive Law: Application to Aircraft Engines". American Society of Mechanical Engineers Digital Collection, pp. 907–916. doi: 10.1115/DETC2009-87669 - oai: hal-00413728.

[27] Agrapart, Q., Nyssen, F., Lavazec, D., Dufrénoy, P., and Batailly, A., 2019. "Multi-physics numerical simulation of an experimentally predicted rubbing event in aircraft engines". *Journal of Sound and Vibration,* **460**, Nov., p. 114869. doi: 10.1016/j.jsv.2019.114869 - oai: hal-02269517.

[28] Castanier, M. P., and Pierre, C., 2006. "Modeling and analysis of mistuned bladed disk vibration: Status and emerging directions". *Journal of Propulsion and Power,* **22**, pp. 384–396. doi: 10.2514/1.16345.

[29] Choi, B.-K., Lentz, J., Rivas-Guerra, A., and Mignolet, M., 2002. "Optimization of intentional mistuning patterns for the reduction of the forced response effects of unintentional mistuning: formulation and assessment". *J. Eng. Gas Turbines Power,* **125**(1), pp. 131–140. doi: 10.1115/1.1498270.

[30] Beirow, B., Figaschewsky, F., Kühhorn, A., and Bornhorn, A., 2019. "Vibration analysis of an axial turbine blisk with optimized intentional mistuning pattern". *Journal of Sound and Vibration,* **442**, pp. 11–27. doi: 10.1016/j.jsv.2018.10.064.

[31] Ewins, D., 1969. "The effects of detuning upon the forced vibrations of bladed disks". *Journal of Sound and Vibration,* **9**(1), pp. 65–79. doi: 10.1016/10.1016/0022-460X(69)90264-8.

[32] Whitehead, D., 1966. "Effect of mistuning on the vibration of turbo-machine blades induced by wakes". *Journal of Mechanical Engineering Science,* **8**(1), pp. 15–21. doi: 10.1243/JMES_JOUR_1966_008_004_02.

[33] Ottarsson, G., and Pierre, C., 1995. "On the effects of interblade coupling on the statistics of maximum forced response amplitudes in mistuned bladed disks". In 36th Structures, Structural Dynamics and Materials Conference. doi: 10.2514/6.1995-1494.

[34] Hodges, C., 1982. "Confinement of vibration by structural irregularity". *Journal of Sound and Vibration,* **82**(3), pp. 411–424. doi: 10.1016/S0022-460X(82)80022-9.

[35] Pierre, C., 1988. "Mode localization and eigenvalue loci veering phenomena in disordered structures". *Journal of Sound and Vibration,* **126**(3), pp. 485–502. doi: 10.1016/0022-460X(88)90226-X.

[36] Ottarsson, G., and Pierre, C., 1993. "A transfer matrix approach to vibration localization in mistuned blade assemblies". In ASME International Gas Turbine and Aeroengine Congress and Exposition. Volume 2: Combustion and Fuels; Oil and Gas Applications; Cycle Innovations; Heat Transfer; Electric Power; Industrial and Cogeneration; Ceramics; Structures and Dynamics; Controls, Diagnostics and Instrumentation; IGTI Scholar Award. doi: 10.1115/93-GT-115.

[37] Klauke, T., Kühhorn, A., Beirow, B., and Golze, M., 2009. "Numerical investigations of localized vibrations of mistuned blade integrated disks (blisks)". *Journal of Turbomachinery,* **131**(3), p. 031002. doi: 10.1115/1.2985074.

[38] Castanier, M. P., Ottarsson, G., and Pierre, C., 1997. "A Reduced Order Modeling Technique for Mistuned Bladed Disks". *Journal of Vibration and Acoustics,* **119**(3), 07, pp. 439–447. doi: 10.1115/1.2889743.

[39] Yang, I.-T., and Griffin, J. H., 1997. "A reduced order approach for the vibration of mistuned bladed disk assemblies". *Journal of Engineering for Gas Turbines and Power,* **119**, pp. 161–167. doi: 10.1115/95-GT-454.

[40] Lim, S.-H., Bladh, R., Castanier, M. P., and Pierre, C., 2007. "Compact, generalized component mode mistuning representation for modeling bladed disk vibration". *AIAA Journal,* **45**(9), pp. 2285–2298. doi: 10.2514/1.13172.

[41] Philippe, J., Thouverez, F., Blanc, L., and Gruin, M., 2018. "Vibratory behavior prediction of mistuned stator vane clusters: An industrial application". *Comput. Struct.,* **196**, pp. 12–23. doi: 10.1016/j.compstruc.2017.11.003.

[42] Wan, H.-P., Ren, W.-X., and Todd, M., 2020. "Arbitrary polynomial chaos expansion method for uncertainty quantification and global sensitivity analysis in structural dynamics". *Mech. Syst. Sig. Process.,* **142**, p. 106732. doi: 10.1016/j.ymssp.2020.106732.

[43] Dreau, J., Magnain, B., Nyssen, F., and Batailly, A., 2021. "Polynomial chaos expansion for permutation and cyclic permutation invariant systems: Application to bladed disks". *Journal of Sound and Vibration,* **503**, p. 116103. doi: 10.1016/j.jsv.2021.116103.

[44] Petrov, E., and Ewins, D. J., 2005. "Method for analysis of nonlinear multiharmonic vibrations of mistuned bladed disks with scatter of contact interface characteristics". *Journal of Turbomachinery,* **127**, pp. 128–136. doi: 10.1115/1.1812781.

[45] Panning, L., Sextro, W., and Popp, K., 2007. "Spatial dynamics of tuned and mistuned bladed disks with cylindrical and wedge-shaped friction dampers". *International Journal of Rotating Machinery,* **9**, pp. 219—-228. doi: 10.1155/S1023621X03000198.

[46] Pourkiaee, M., and Zucca, S., 2018. "Reduced order model for nonlinear dynamics of mistuned bladed disks with shroud friction contacts". *Journal of Engineering for Gas Turbines and Power,* **141**, p. 011031. doi: 10.1115/GT2018-75223.

[47] Zhao, W., Zhang, D., and Xie, Y., 2019. "Vibration analysis of mistuned damped blades with nonlinear friction and contact". *Journal of Low Frequency Noise, Vibration and Active Control,* **38**(3-4), pp. 1505–1521. doi: 10.1177/1461348419836352.

[48] Joachim, J., Nyssen, F., and Batailly, A., 2020. "Numerical Investigation of a Mistuned Academic Bladed Disk Dynamics with Blade/Casing Contact". *Journal of Engineering for Gas Turbines and Power*, July. doi: 10.1115/1.4047780 - oai: hal-02896893.

[49] Nyssen, F., and Batailly, A., 2021. "Investigation on the robustness of rotor/stator contact interactions with respect to small mistuning". In Proceedings of the ASME 2021 Turbo Expo conference, ASME. doi: 10.1115/GT2021-59216 - oai: hal-03286203.

[50] Colaïtis, Y., and Batailly, A., 2021. "The harmonic balance method with arc-length continuation in blade-tip/casing contact problems". *Journal of Sound and Vibration,* **502**, p. 116070. doi: 10.1016/j.jsv.2021.116070 - oai: hal-03163560.

[51] Carpenter, N., Taylor, R., and Katona, M., 1991. "Lagrange constraints for transient finite element surface contact". *International Journal for Numerical Methods in Engineering,* **32**(1), pp. 103–128. doi: 10.1002/nme.1620320107.

[52] Craig, R., and Bampton, M., 1968. "Coupling of substructures for dynamic analysis". *American Institute of Aeronautics and Astronautics Journal,* **6**(7), pp. 1313–1319. doi: 10.2514/3.4741.

[53] Batailly, A., Meingast, M., and Legrand, M., 2015. "Unilateral contact induced blade/casing vibratory interactions in impellers: Analysis for rigid casings". *Journal of Sound and Vibration,* **337**, February, pp. 244–262. doi: 10.1016/j.jsv.2014.10.010 - oai: hal-01120157.

[54] Bladh, R., 2001. "Efficient predictions of the vibratory response of mistuned bladed disks by reduced order modeling". PhD thesis, University of Michigan. oai: tel-00358168.

[55] Joachim, J., 2020. "Développement de modèles numériques de roues aubagées désaccordées dans un contexte non-linéaire [Development of numerical models of mistuned bladed disks in a nonlinear context]". PhD thesis, Ecole Polytechnique de Montréal, June. oai: tel-02888893.

[56] Groll, G. V., and Ewins, D., 2001. "The harmonic balance method with arc-length continuation in rotor/stator contact problems". *Journal of Sound and Vibration,* **241**(2), pp. 223–233. doi: 10.1006/jsvi.2000.3298.

[57] Salles, L., Gouskov, A. M., Blanc, L., Thouverez, F., and Jean, P., 2010. "Dynamic Analysis of Fretting-Wear in Joint Interface by a Multiscale Harmonic Balance Method Coupled With Explicit or Implicit Integration Schemes". American Society of Mechanical Engineers Digital Collection, pp. 1003–1013. doi: 10.1115/GT2010-23264.

[58] Millecamps, A., Brunel, J.-F., Dufrénoy, P., Garcin, F., and Nucci, M., 2010. "Influence of Thermal Effects During Blade-Casing Contact Experiments". American Society of Mechanical Engineers Digital Collection, pp. 855–862. doi: 10.1115/DETC2009-86842.